UAS-Acquired High-Resolution Aerial Imagery-Based Modeling of Artificial Flood Zones

Final Report for the Marshall Plan Foundation

By:

Daniel Beene
University of New Mexico
Department of Geography and Environmental Studies

Supervisor at Host University:

Mag. Dr. Gernot Paulus, MSc., MAS
FH-Professor
Carinthia University of Applied Sciences
Villach, Austria

Supervisor at Home University:

Dr. Su Zhang, Ph.D.
Earth Data Analysis Center
University of New Mexico
Albuquerque, New Mexico

November 2018

Acknowledgements

Among the many people who generously supported my research, I am compelled to acknowledge Dr. Su Zhang at the University of New Mexico for his guidance in developing this project and Dr. Gernot Paulus at the Carinthia University of Applied Science (CUAS) for helping me refine my questions and successfully complete my research, and both for their continued guidance. I would also like to thank the faculty and staff at CUAS for their warm welcome, and willingness to connect me to rich learning and cultural opportunities. Finally, I extend sincere thanks to the Austrian Marshall Plan Foundation, without whose financial support this research would not have been possible.

Abstract

This research presents a conceptual workflow for the appropriate processing of high-spatial resolution small unmanned aircraft system (sUAS) data for hydrologic modeling of floodplains during flooding events. A digital surface model (DSM) and co-registered orthophoto mosaic of a stretch of the Drau River in southern Austria is generated using structure-from-motion. Next, a digital terrain model (DTM) is approximated from the generated DSM to within a reported vertical root-mean-square error (RMSE) of 4.65 cm. Two generally-accepted metrics of surficial roughness, horizontal and random roughness, are used to determine spatially-varying values of Manning's *n* coefficient across the observed floodplain. A distributed two-dimensional hydrologic model of a river channel and simulated floodplain is performed using two-dimensional hydraulic modeling software. The effectiveness of each roughness metric at multiple pixel resolutions to model significant variations in reported maximum velocity, water surface elevation, and maximum depth during a flood event is tested in a controlled sensitivity analysis. Results indicate that accuracy in hydrologic modeling is impacted by scale. However, pixel resolution is not necessarily a reliable indicator of precise estimation of velocity, depth, and water surface elevation. We conclude by emphasizing the importance of context in hydrologic modeling scenarios to effectively meet the needs of end users.

Contents

1. Introduction

Unpredictable environmental events can have profound effects on a variety of infrastructural networks. As societies modernize, infrastructure interdependence extends to all corners of human-occupied space (Chou and Tseng, 2010; Leavitt & Kiefer, 2006; Ouyang, 2014; Robert, Senay, Plamondon, and Sabourin, 2003). This expansion of interdependence increases the odds of cascading effects of failure, rendering processes of public health and safety, economic stability, and quality of life subject to the resilience of manmade systems at an array of scales.

Therefore, understanding the resilience and interdependence of critical infrastructure systems (CIS) in terms of planning and decision support is crucial. While a substantial body of research focuses on this field, accessing to high quality data presents a fundamental problem in fully modernizing resilience measures globally (Ouyang, 2014). Access to relevant topological data necessary to model critical infrastructure can be limited by reasons ranging from confidentiality and privacy issues to antitrust rules or reluctance toward sharing (Robert, Senay, Plamondon, and Sabourin, 2003).

The research presented in this paper focuses on water transport as a discrete yet important component in critical infrastructure systems (CIS) (Ouyang, 2014). Furthermore, we seek to develop a holistic hydrologic and flood-prediction model using only aerial imagery derived from unmanned aerial systems (UAS). The primary benefit of using UAS imagery is cost effectiveness in comparison to potentially-prohibitive data acquisition methods, such as LiDAR. This cost benefit can have implications in terms of a wider user pool and social equity for underprivileged communities.

Understanding the behavior of water across CIS can help support the resilience of communities and resource networks in responding to flood events and in managing economic processes. López et al. (2017) utilized satellite-based soil moisture data to develop hydraulic models of underrepresented world regions and they concluded that in situ data collection is still required to produce ideal results. In recognizing the limitation of obtaining robust and accurate datasets, this research leverages the increased modern availability of UAS for high-spatial resolution aerial imagery acquisition and structure-from-motion (SfM) techniques to accurately model channels and overland flow across floodplains. Overland flow is associated with sediment and pollutant transport and is an efficient driver of erosion and infrastructure damage (Zhang, Liu, Li, and Liang, 2016). The transport of water therefore has clear implications in the resilience of CIS.

Numerous workflows exist in the utilization of UAS in acquisition and photogrammetric modeling of landforms and the criteria for hydraulic modeling are clearly defined by the functional requirements of modeling software. The aim of this research is to unite these two concepts into one roadmap by presenting a workflow to conceptualize a theoretical floodplain using UAS acquired data. It will include UAS-based high-spatial resolution aerial data acquisition, SfM digital terrain model (DTM) estimation from a digital surface model (DSM), and calculation and sensitivity analysis of two roughness indices in a distributed 2D hydrologic model.

2. Background

The acquisition and utilization of UAS data for earth resources monitoring is not new, and contemporary workflows for hydrologic modeling using high-spatial resolution aerial imagery do exist as well. In recent years, UAS has emerged as an important platform for collecting high-spatial resolution aerial imagery.

These aerial images have been used to observe and model temporal variations in river stages (Niedzielski et al.,2016), support ecohydrology (Vivoni et al., 2014), and study the runoff behavior of water across impervious surfaces (Tokarczyk et al., 2014). Langhammer et al. (2017) present a coupled model of UAV imagery and an automated sensor network to develop a hydrodynamic flood model across variable terrain. This research, however, is positioned to decouple UAS data from other data sources, including sensor networks and LiDAR, to model the effect of topographic variability on hydraulic flux in terms of roughness, pooling, and absorption or overland flow.

Mathematical models of hydraulic behavior in channels and across floodplains are used by a diverse array of researchers and decision-makers to typify and predict a diverse array of flow scenarios. It relies on quantifying the known behavior of water at various levels of turbidity and temperatures as it interacts with the pedosphere – the outermost skin of the earth upon and through which water, energy, and nutrients are exchanged. Naturally, the role of the pedosphere in hydraulic flux is a crucial and well-studied factor in hydrologic modeling, but the computational capabilities of established mathematical models are subject to technologic limitations (Clark et al., 2017). The rising dominance of UAS in local-scale environment surveying campaigns presents both a wealth of information-rich datasets and a new set of problems pertaining to the ability of existing models to use such detailed and enormous amounts of information. Indeed, UAS are more accessible than light detection and ranging (LiDAR) or ground survey systems in terms of cost efficiency and ease of use, but their inherent ability to capture discrete and small-scale variations in radiometric resolution and elevation of earth's surface has not been well-explored in system-wide hydraulic models.

Along with accurate DTMs of a given study area, one of the most important considerations in hydrologic models is roughness, which has been quantified in many ways, at times leading to debate among experts (Zhang et al., 2016). Surficial roughness is dependent on land cover type and relative variation in height across space. Differences in land cover type that affect roughness can be captured by deterministic models of flow, such as the Darcy-Weisbach friction factor or the Manning coefficient (Taconet and Ciarletti, 2007), which categorize observable characteristics of land use or land cover and assign a constant coefficient based on empirical observation of channels and floodplains (Chow, 1959) or vegetative density (Copeland, 2000; Freeman et al., 1998).

Zhang et al.(2016) provide a detailed discussion of hydrologic modeling as it pertains to overland flow pointing to limitations inherent in characterizing roughness in distributed hydrologic models. Because roughness is dependent on physical system characteristics, such as boundaries, flow velocity, water depth, and properties of excess overland infiltration that are by their very nature environmentally-dependent, holistic representation of overland and channel flow is limited by the sheer magnitude of contributing factors (Clark et al., 2017). Despite this innate constraint, a wealth of studies aimed at modeling these factors provide a basis upon which further modeling paradigms can develop. These studies have been classified into three types (Zhang et al., 2016). The first assume that roughness affects volume, velocity, and flood peaks during runoff. The second type models roughness as spatially-varying according to land use and land cover (e.g. Luo et al., 2017). Finally, the third type considers spatial variability of roughness on a cell-by-call basis.

The quantification of roughness has roots in the 19th century. Manning's equation was developed by Irish engineer Robert Manning in 1889 as an alternative to the then-common Chezy equation. It is

designed to quantify uniform flow in an open channel as a function of the channel velocity, flow area, and slope as follows:

$$Q = VA = \left(\frac{1.00}{n}\right) AR^{\frac{2}{3}}\sqrt{S} \qquad (1)$$

Where *Q* is the flow rate in cubic meters per second, *V* is velocity in meters per second, *A* is area in square meters, *n* is the roughness coefficient, *R* is the hydraulic radius in meters, and *S* is the slope in meters per meter. Chow (1959) published a comprehensive table of *n* values that typifies the coefficient for various channel and land cover characteristics along a spectrum ranging from minimum to maximum values for each type. Roughness is still commonly represented in terms of Manning's *n* in computational hydraulic models, including the U.S. Army Corps of Engineers Hydraulic Engineering Center River Analysis System (HEC-RAS) and the iRIC Project.

However, because flow velocity and direction are dependent on water depth, there have been numerous attempts to characterize small-scale roughness to model hydrologic processes across tilled soil for agricultural purposes (Allmaras et al., 1966; Govers et al., 2000; Kamphorst et al., 2000; Marzahn and Ludwig, 2009; Marzahn et al., 2012). The consensus of these studies is that water pooling in interrill regions of farm catchments and small-scale variation in roughness affects system-wide flow. These studies present a solid foundation in understanding the most apropos methods for developing dynamic hydrologic models that respond to anthropogenic action and weather influences. Prior to advanced high-resolution photogrammetric or laser scanning techniques, roughness was described by two primary indices: random roughness (Allmaras et al., 1966; Currence and Lovely, 1970) and tortuosity (Boiffin, 1984; Taconet and Ciarletti, 2007).

According to Allmaras (1966), random roughness is essentially the standard error of measured heights across a surface. Marzahn, Rieke-Zapp, and Ludwig (2012) compute random roughness (*s*) for a micro-scale DEM of tilled soil as the standard deviation of the heights (*Z*) to a reference height ($\bar{Z}$):

$$s\ (cm) = \sqrt{\frac{\sum_{i=1}^{n}(Z_i - \bar{Z})^2}{n-1}} \qquad (2)$$

Therefore, random roughness can effectively conceptualize the variation of a topographic position of each measured value or pixel in a DEM.

Characterization of surface roughness for tilled soil has traditionally understood roughness to be isotropic, or directionally-dependent. In order to capture the parallel structure of rills in ploughed soil, random roughness and tortuosity (Boiffin, 1984; Taconet and Ciarletti, 2007) were typically described as a relationship between horizontal and perpendicular measurements of height values across a surface. Anisotropy of roughness has been observed as scale increases (Blaes and Defourny, 2008) and researched at the watershed level (Zhang and Liu, 2017). However, Marzahn, Reike-Zapp, and Ludwig (2012) demonstrate that roughness is anisotropic even at small scales and is therefore captured in a more robust way by omnidirectional spatial autocorrelation of height values. They proposed fitting a theoretical variogram ($\tilde{\gamma}$) of height values across space to the observed variogram ($\hat{\gamma}$) to determine the distance at which the autocorrelation function (ACF) tapers off exponentially – this value was shown to effectively represent the relationship between height values across planar space. This implies a logical relationship between directional dependence of roughness and spatial variation of land cover as demonstrated by Zhang, Liu, Zhang, Liu, and Wang (2018).

Furthermore, it has been conclusively demonstrated that overall surface roughness is inherently scale-dependent (Davidson et al., 2000; Marzahn and Ludwig, 2009; Taconet and Ciarletti, 2007; Verhoest et al., 2008). Taconet and Ciarletti (2007) introduced an approach to measure relative accuracy in the selection of an optimal DSM size. However, this method is limited by the antiquated assumption that roughness is isotropic. To address this limitation, Marzahn, Reike-Zapp and Ludwig (2012) proposed the relative elementary area (REA) which utilizes a moving window to smooth elevation values to a threshold where accuracy between a theoretical and observed model of roughness is maximized.

Current attempts to model roughness across variable terrain rely on detailed land cover and land use classification and application of established Manning's *n* values. Dorn et al. (2014) explored the utility of LiDAR, volunteered geographic information (i.e., OpenStreetMap), and CORINE land cover datasets along with object based image analysis (OBIA) for roughness parametrization to capture overland during theoretical flood scenarios. However, there is little research into the methods of using established roughness indices to inform the selection of Manning's *n* coefficient based on their listed ranges.

3. Study Area

Data was acquired on November 4, 2016, over the Drau River near Obergottesfeld in Carinthia, Austria. The Drau River through the Obergottesfeld Valley is part of the first EU-sponsored LIFE Project aimed at monitoring restoration of riparian habitat and wetland areas along its bank. Extensive railroad development, channel realignment, and reduced gravel and sediment dredging throughout the 19th century exacerbated erosion along the banks of the river, threatening both ecological services and agriculture (Lebensader Obere Drau, 2011). The dynamic history of varied use and continued monitoring of this stretch of the river make it a good proxy for many modern managed rivers worldwide.

There are many farms along the Drau which grow a variety of crops, including corn, wheat, peas, and alfalfa. These farms rely on predictably frequent rain events and efficient overland flow and seepage, though there is growing concern over the last two decades that climate change is redistributing precipitation patterns and groundwater recharge (Auer et al., 2011). The Drau River, which spans Italy, Austria, Slovenia, Croatia, and Hungary, is one of the largest tributaries of the Danube. Significant flooding along the Drau River, while uncommon in modern times, is not unheard of – large water releases from Austria in 2012, for example, led to a disruptive flood event in Slovenia that damaged homes and farms in its path ("Drava River Floods Hundreds of Homes," 2012).

Specifically, the study area (Figures 1 and 2) is an approximately 1.4-kilometer-long tract along the Drau River adjacent to Obergottesfeld. The primary landcover types in the scene are early growth agriculture, senesced and dispersed evergreen vegetation, bare soil in the form of roads and footpaths, silt deposits along riverbanks, exposed rock, and open water. For use as a proof-of-concept model and to alleviate computational requirements, the scene was significantly subset to 268 by 107 meters (which corresponds to 40 tiles of 1024 x 1024 pixels) that were representative of the primary landcover types in the overall scene.

Figure 1: Study area map.

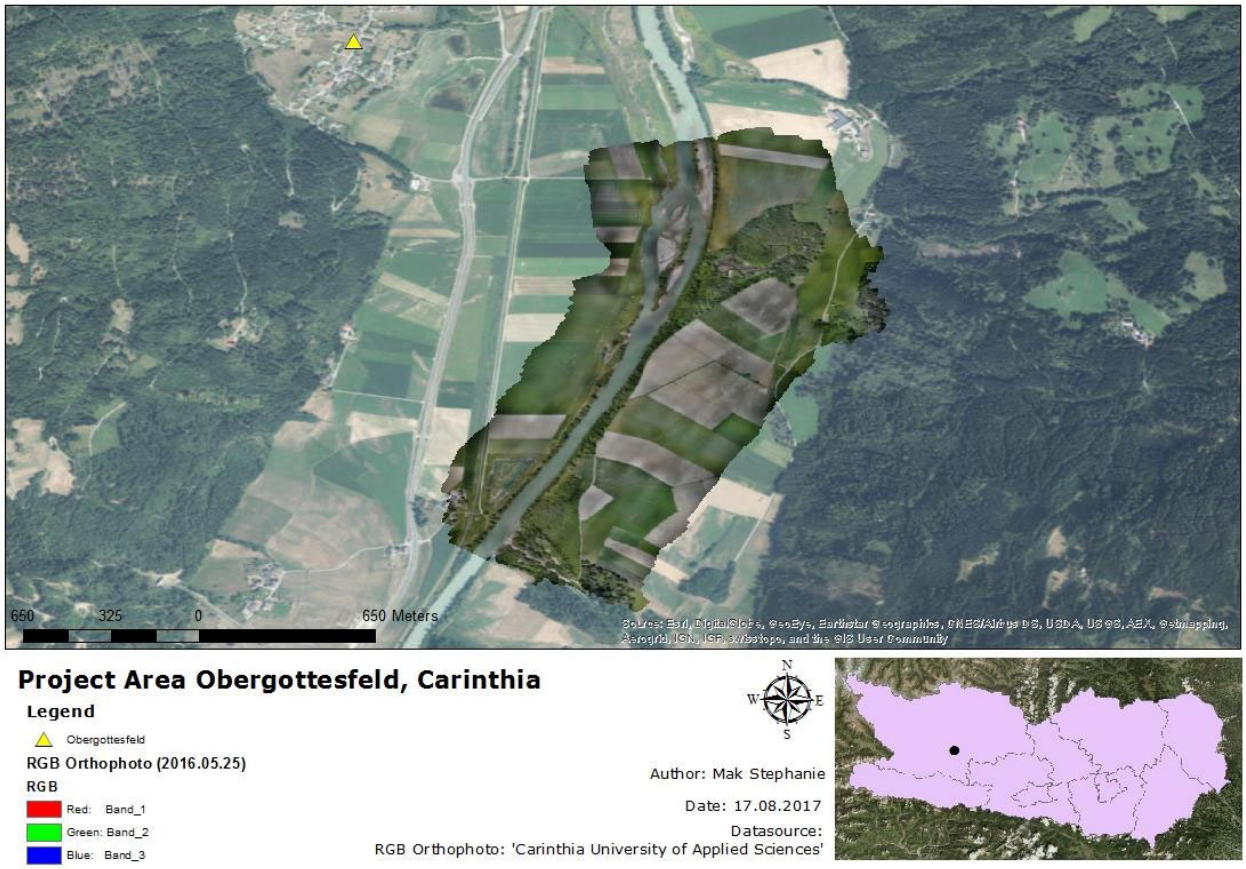

Figure 2: In situ depiction of test site.

4. Methods

4.1. Overview of Conceptual Model/Structure

This research presents a conceptual workflow for the use of high-spatial resolution UAS aerial imagery in hydrologic modeling. It focuses primarily on data post-processing and hydrologic modeling in a computational environment. Figure 3 demonstrates the general structure of the proposed workflow.

Figure 3: Proposed workflow.

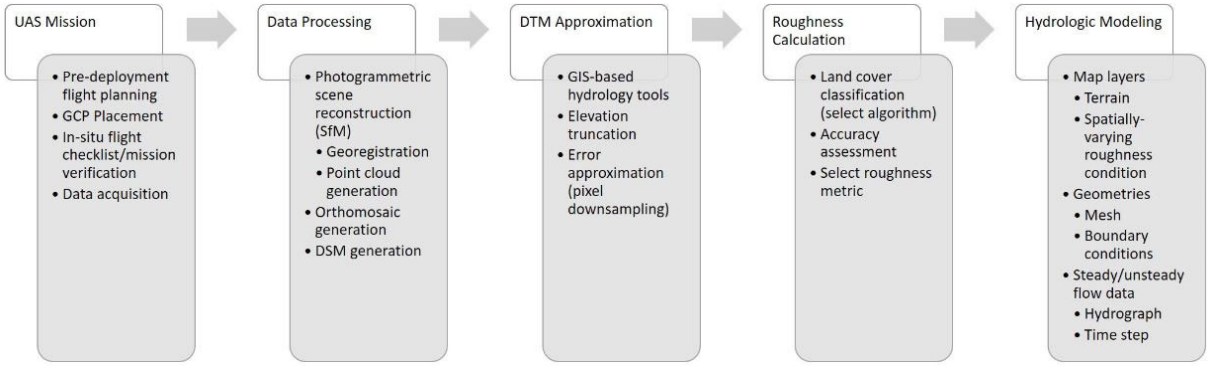

This conceptual workflow is designed to manage UAS-acquired high-spatial resolution aerial imagery for its use in 2D hydrologic models, specifically HEC-RAS. Upon completion of post-processing these data, an artificial floodplain is simulated using a theoretical hydrograph with a logarithmic shape peaking at 1339.598 cubic meters per second (cms). This peak flow was determined to sufficiently inundate the entire study area.

The most rudimentary requirements to conduct 2D hydraulic modeling are elevation and roughness layers and a mesh across which water flux is approximated. We predicted a DTM from a digital surface model (DSM) derived by SfM of aerial imagery using tools available in the ArcGIS Spatial Analyst extension to a degree of accuracy within 4.65 cm root-mean-square error spatial variation from a LiDAR DTM. A three-band red-green-blue (RGB) digital orthophoto of the scene was classified through a series of remote sensing vegetation indices and K-means unsupervised classification to inform spatial variability of Manning's *n* roughness coefficients which were then calibrated two common roughness indices: random and horizontal roughness. A sensitivity analysis compares each roughness index at multiple pixel resolutions, revealing the most statistically-significant measure of roughness to be scale-dependent, with trends indicating that horizontal roughness with smaller pixel size tend to predict variance of water surface elevation and maximum water depth, but that maximum velocity is harder to pin down.

4.2. UAV Mission

4.2.1. Acquisition Setup

Data sampling was conducted using a Bramor ppX (Figure 4) developed by the Slovenian company, C-Astral Aerospace Ltd. Autonomous navigation, gliding, takeoff, and landing was managed by Procerus

Technologies' Kestrel autopilot system. A total of 838 images with 70% overlap and 70% sidelap were captured using a Sony a6000 RGB sensor.

Figure 4: CUAS pilot Melanie Erlacher launching Bramor ppX UAS.

4.3. Data Processing

Digital orthophotography and the digital surface models (DSMs) were generated using Agisoft PhotoScan (Version 1.4) software. Agisoft is a robust photogrammetry tool that uses epipolar constraints from a set of stereo images to establish the exterior orientation of input imagery – a process now commonly referred to as structure-from-motion (SfM) (Agisoft LLC, 2018; Marzahn et al., 2012). By associating imagery to ground control points (GCPs), the three-dimensional (3D) structure of objects and elevation values was calibrated using SfM. Digital orthophotos are then mosaicked into a continuous scene co-registered to the DSM.

4.4. DTM Approximation

It is necessary to accurately model the surface upon which water flows. However, the generation of these models from four-band aerial imagery may understandably be limited by the presence of vegetation which precludes the reflection of electromagnetic radiation from the sub-canopy surface. LiDAR is an effective technique to address this, as light pulses from active sensors effectively pass through the gaps between vegetation, resulting in staggered rates of return to a sensor whereby more accurate models of topographical structure may be developed. However, the high cost of LiDAR acquisition can be prohibitive in certain modeling scenarios.

The proposed DTM approximation method relies on commonly-available GIS hydraulic algorithms designed to fill data sinks in DTM. Typically, the Fill function in ArcMap is used to identify individual pixels or small groups of pixels with height values that vary drastically from those of their immediate neighborhood. It can be used to remove peaks or depressions that generally result from spurious digital

number (DN) values in a raster surface. A threshold value of maximum or minimum elevation values can also be specified in the fill tool to define the point at which those values may be truncated.

The first step of the workflow is to invert the DSM so that the maximum and minimum values are swapped – like flipping an egg carton upside-down. This process will allow the Fill tool to interpret superficial features such as vegetation as precipitous sinks in the model and remove those depressions. A DSM is inverted using the following equation:

$$DSM_i = [(DSM - DSM_{max}) \times 1] + DSM_{min} \quad (3)$$

Where DSM_i is the inverted surface, and DSM_{max} and DSM_{min} are the minimum and maximum values of the model, respectively. This new inverted surface was the input raster in the Fill tool. No limits were specified to truncate input elevation values in the tool dialog, but rather, standard deviations of elevations were manually removed to ensure that z limits were restricted to sinks as opposed to peaks. Standard deviations of elevation were removed incrementally to ensure that only superficial features (vegetation) were removed. The results of this sensitivity analysis are discussed later.

4.5. Roughness Calculation

Roughness is commonly defined in terms of Manning's *n* coefficients, which are derived from empirical mathematical observation of characteristics of in-channel and overland flow. Each coefficient is expressed as a range of values (Chow, 1959). The current research focuses on employing two metrics of roughness quantification – horizontal and random roughness – to inform discrete values within those proscribed ranges.

4.5.1. Land Cover Classification

To effectively capture the land cover variation within the scene, a classification scheme was employed using Erdas Imagine (v. 2015). The RGB digital orthophoto was used as the training set for a K-Means unsupervised classification into 36 unique classes with 10 iterations and a convergence threshold of 0.95. K-Means is an algorithm that iteratively clusters pixels based on their spectral characteristics. It will continue to cluster pixels in the scene until either the clustering process repeats or the user-specified maximum number of iterations has been reached.

Initial K-Means classification within these parameters did not effectively distinguish between soil, rock, or vegetation that was submerged in the river channel from features along the floodplain, resulting in an untenable degree of overlap to be considered accurate. To alleviate this, the river channel was manually digitized and extracted from the entire scene prior to the final classification process. The 36 clusters were reclassified into three simple land cover classifications: healthy vegetation, woody biomass or sparse vegetation, and bare soil. Open water, which was manually-digitized, comprised the fourth class.

4.5.2. Horizontal Roughness

Horizontal roughness quantifies the spatial autocorrelation of elevation values across an elevation surface. Based on methods detailed by Marzahn et al. (2012), the autocorrelation length, *l*, was determined for each of the four classes. The initial step is to convert the DSM of the entire scene to points, of which there are more than 40 million. To minimize the computational burden and processing time, the DSM point layer was then subset to 1% of the input points randomly – approximately 410,000 points. Class information was then extracted to each point and four unique point classes were

generated from this attribute extraction. Following Marzahn et al. (2012), the points were further subset to 10,000 points per class using an absolute value to randomly select a specific amount per class.

The semivariance between point pairs at which point autocorrelation drops exponentially was calculated using the global Moran's I statistical test of spatial autocorrelation as follows: 5.593 meters for open water, 6.2747 meters for healthy vegetation, 3.8351 meters for woody biomass and sparse vegetation, and 6.0616 meters for bare soil.

A theoretical variogram with an exponential shape was then calculated for each class based on the concept that autocorrelation drops precipitously in terms of elevation-based roughness (Blaes and Defourny, 2008; Davidson et al., 2000; Marzahn, Rieke-Zapp, and Ludwig, 2012), and is fitted to the experimental variogram, which is defined as:

$$\tilde{\gamma}(h) = \frac{1}{2n}\sum_{i=1}^{n}[Z(x_i) - Z(x_i + h)]^2 \qquad (4)$$

Where $\tilde{\gamma}(h)$ is the variogram, *n* is the number of points observed, and $Z(x_i) - Z(x_i + h)$ defines the spatial relationship between point pairs (Webster and Oliver, 2007).

Next, the ACF ($\tilde{\rho}(h)$) is calculated based on the following ratio:

$$\tilde{\rho}(h) = 1 - \frac{\tilde{\gamma}(h)}{\tilde{\gamma}(\infty)} \qquad (5)$$

Where $\tilde{\gamma}(h)$ is the semivariance distance between two points and $\tilde{\gamma}(\infty)$ is the major range of the semivariogram, or the distance along the semivariogram where the sill tapers off exponentially (Webster and Oliver, 2007).

Each measurement of ACF per class was then used to inform the range of values in the Manning's *n* lookup table per Chow (1959). Manning's *n* values for each classified land cover from the study area were assigned the following classes: clean bottom channel with brush on sides for open water, range from 0.04 to 0.08; medium to dense brush in summer for healthy vegetation, range from 0.07 to 0.16; scattered brush and heavy weeds for woody biomass and sparse vegetation, range from 0.035 to 0.07; and floodplain with no crop for bare soil, range from 0.02 to 0.04. Discrete values were applied according to the equation:

$$n_D = [\tilde{\rho}(h)(n_{max} - n_{min})] + n_{min} \qquad (6)$$

Where n_D is the discrete *n* value, $\tilde{\rho}(h)$ is the ACF, n_{max} is the maximum value in the listed range, and n_{min} is the minimum value.

4.5.3. Random Roughness

The random roughness metric characterizes roughness of a surface in terms of local variation of elevation values across a surface. As such, it can be used to simply apply a roughness value per pixel within each derived class. The relationship between each pixel is expressed in terms of standard deviations of elevation across the entire surface.

The standard deviation of each pixel relative to its immediate neighborhood in a 3 x 3 moving window was calculated using the topographic position index (TPI) (Jenness, 2013). TPI is a tool that classifies landscape into a topographic position at different scales and into different classes of landforms. The

topographic position of a pixel is the difference between a cell's elevation value and the average elevation values of the neighboring cells. It can be expressed in terms of elevation units (meters or feet) or standard deviations.

Next, the standard deviation surface, which ranges in values from -2.67 to 2.53, was added to the original DSM, creating a standard deviation height surface. An elevation error raster surface was then generated according to the equation:

$$S = \sqrt{\frac{\sum_{i=1}^{n}(z_i - \bar{z})^2}{n-1}} \qquad (7)$$

Where z_i is the standard deviation height and $\bar{z}$ is the reference height (mean value of the original DSM).

The values from the standard deviation surface were then associated with each of the four classes by relating class information from the thematic raster layer to the random roughness surface. Finally, to associate the random roughness values to Manning's *n* coefficients, they were normalized to a range from 0 to 1 and multiplied by the same four ranges as in the horizontal roughness step. Each pixel in the scene was then represented by a floating value somewhere between the proscribed *n* coefficient. However, HEC-RAS can only handle up to 256 integer values, so random roughness was reclassified to a range from 0 to 255 and the raster was converted to integer format.

4.6. Hydrologic Modeling

To assess the degree to which scale in terms of pixel size affects the results of hydraulic modeling, a series of simulations were run using both horizontal and random roughness layers at pixel sizes ranging from 2 cm to 100 cm. Simulations were conducted using HEC-RAS version 5.0. HEC-RAS is a publicly-available software developed by the U.S. Army Corps of Engineers that allows end users to conduct one-dimensional (1D) steady flow simulations, and one- and two-dimensional (2D) unsteady flow simulations. It also enables water temperature and quality analysis through simulations of sediment transport.

Every scenario under which roughness was calibrated in the sensitivity analysis remained static regarding all other model inputs. The environments utilized are described in the following sections.

4.6.1. Map Layers

Map layers in the HEC-RAS modeling software are similar in structure and function to a GIS environment. Terrain is modeled accordingly from an elevation raster whereby elevation values are rendered in three dimensions. The DTM generated prior to building the hydraulic model remained unchanged during the sensitivity analysis.

4.6.2. Geometries

Geometric inputs in the hydrologic analysis include vector-based data which, when interpreted in the modeling process, serve as a set of topological rules that enable or restrict flow of water across the raster surface. These topological rules are essentially determined by the nature of a mesh structure. A mesh is initially defined by the 2D flow area to be computed in the modeling procedure. It is comprised of a cell center, cell faces, and cell face points. The cell center is the computational point where the water surface elevation is calculated for each cell. It is not necessarily the centroid of the cell, which

varies according to the structure of cell faces – the delineated boundaries of any computational cell. Cell faces are typically straight lines but may be multipoint line features. Finally, cell face points are the nodes either at cellular junctions or at the extent of the 2D flow area. Features are defined according to the names of each cell face point (U.S. Army Corps of Engineers, 2016).

The smallest possible mesh size to be used in conjunction with the input data frame was one meter by one meter. The 2D flow area was defined as a rectangle with cell centers corresponding exactly to each cell centroid. Cross-sectional boundary conditions were drawn across the nodes corresponding with the upstream and downstream portions of the Drau in the scene to model the inflow and outflow, respectively. No break lines of additional features were drawn.

4.6.3. Unsteady Flow Approximation

Hydrographs plot river discharge in volume units over time and are used to display change in river flow during observable events. Storm hydrographs tend to peak after a rainfall event with the rising limb of inundation representing a waterway's response to increased flow discharge. Peak discharge is the point at which flows begin to decrease into the recessional decay limb.

A theoretical hydrograph was developed to simulate a flash flood event with sufficient magnitude to overtop the riverbanks and inundate adjacent farmland. The average base flow of the Drau is two cubic meters per second (m^3s^{-1}) (Achleitner and Rauch, 2006). The theoretical hydrograph reports flow in m^3s^{-1} at the inflow location every 10 minutes. The first three reported flow levels represent the average base flow and then increase along a logarithmic function to 1383 m^3s^{-1}, at which point a potentially-destructive flood was simulated. As a point of reference, flooding along the Drau in northern Slovenia reported flows of up to 3100 m^3s^{-1} ("Drava River Floods Hundreds of Homes," 2012). Decay of water levels in the theoretical hydrograph occurred exponentially quicker than the rising limb so that the behavior of pooling water could be observed in each model iteration.

To isolate the relationship between roughness parameterization and hydraulic behavior during a flood event, the only dynamic variable in each iteration is roughness. Each roughness index – random and horizontal – was modeled at pixel resolutions ranging from 2 cm (the original pixel size) to 100 cm in increments of 14 cm. A stable model of uniform roughness (n = 1) was performed as a baseline against which sensitivity could be assessed.

To reduce approximation error in modeling, relatively simplistic parameters were set and applied uniformly across all model iterations during the sensitivity analysis. To wit, the DTM generated from the DSM, the mesh drawn as a simple rectangle structure of 27664 one meter square cells (the smallest possible size), river inflow and outflow boundary conditions drawn as straight linear cross sections, and the same theoretical flash flood hydrograph remained unchanged in all tests. Figure 5 displays a sample of the two-dimensional mesh over the two centimeter horizontal roughness surface.

Figure 5: 2-D mesh over roughness layer with inflow and outflow boundary conditions across the river.

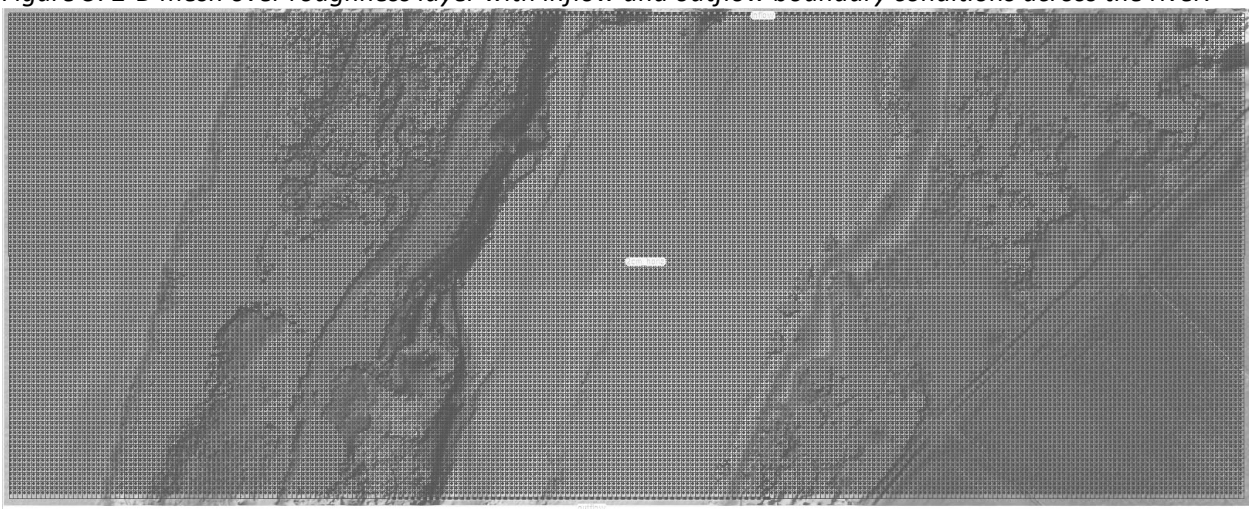

Unsteady flow data for each simulation was based on the above mesh, where the outflow boundary condition line is defined by normal depth, which is derived based on channel slope approximated from aerial imagery as 0.0063°. The hypothetical flash flood flow hydrograph (Figure 6) defined the inflow boundary condition. The data time interval by which flow in cubic meters per second was measured is 10 minutes. A total of 130 measurements were calculated in each scenario.

Figure 6: Hydrograph of hypothetical flash flood scenario used in all simulations.

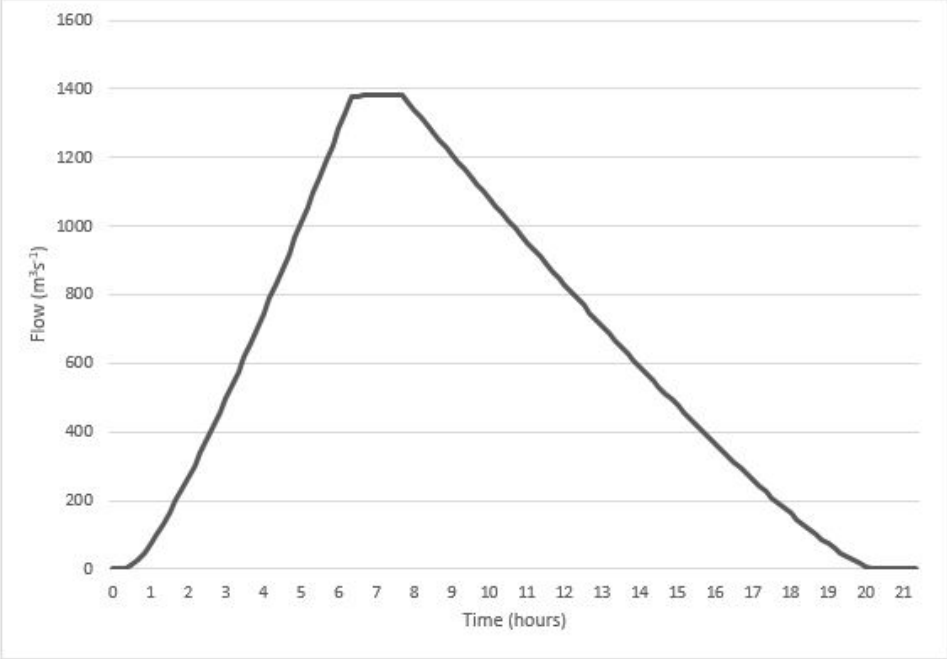

The simulation was tested a total of 17 times under the following conditions: horizontal and random roughness at 2cm, 16cm, 30cm, 44cm, 58cm, 72cm, 86cm, and 100cm, and one control condition of uniform roughness (n = 1) across the entire scene. Measurements of water surface elevation (WSE), maximum depth, and maximum velocity were taken at 30-second computational intervals in an unsteady flow analysis.

To generate the roughness layers with down-sampled pixel resolution, cells were resampled in the HEC-RAS mapper, which derives raster values per cell based on nearest neighbor sampling. Four classes of *n* values were input into each measurement of horizontal roughness and 256 classes were used for each random roughness surface. Every roughness layer was loaded into one central RAS Mapper document and selected individually in the document's geometry properties for each respective simulation. The *n* = 1 simulation was automatically calculated by deselecting all roughness layers in the model.

5. Results

Nearly every stage of the hierarchical workflow presented in this paper incorporates a degree of accuracy estimation or sensitivity analysis prior to proceeding onto the next step. Each of these procedures is described in detail below.

5.1. DTM Validation

The minimum value of the filled raster is 568.8800659 meters and the standard deviation is 1.589983289 meters. We find that truncating the uppermost limits of elevation in the approximated surface increased accuracy in terms of RMSE compared to an existing LiDAR dataset of the study area. The threshold of error was identified through a sensitivity analysis. Six new rasters were calculated to raise minimum elevations to limits defined by one quarter, one half, one, two, three, and four standard deviations less than the original minimum value.

An existing LiDAR dataset was obtained from the Carinthia GIS service, KAGIS, a clearinghouse and repository of geospatial data of the Austrian state of Carinthia. After sub-setting the LiDAR dataset to the study area it was apparent that a conflicting geoid was utilized in the data acquisition and requisition, resulting in elevation values approximately 9.828 meters below those of the UAS data. While it is generally untenable to correct geoidal variation by adding a constant discrete value to all elevations, the curvature of the globe and geoid did not appear to affect elevation variation across the scene at the observed resolutions. A random stratified sample of 15 points classified as bare soil confirmed this. The one-meter pixel resolution of the LiDAR dataset was resampled to mirror the two-centimeter resolution of the UAS scene using the nearest neighbor interpolation technique, whereby no new values were approximated.

After the six filled raster datasets were inverted back to normal, the root-mean-square error (RMSE) was calculated between each individual scene and the resampled and geoid-corrected LiDAR scene. The filled DSM with one standard deviation truncation demonstrated the best fit with a RMSE of 1.767 pixels, or 4.65 cm. Figure 7 is a plot of RMSE related to each input in the sensitivity analysis.

Figure 7: Plot of root-mean-square error of variation between estimated digital terrain model (DTM) and LiDAR DTM

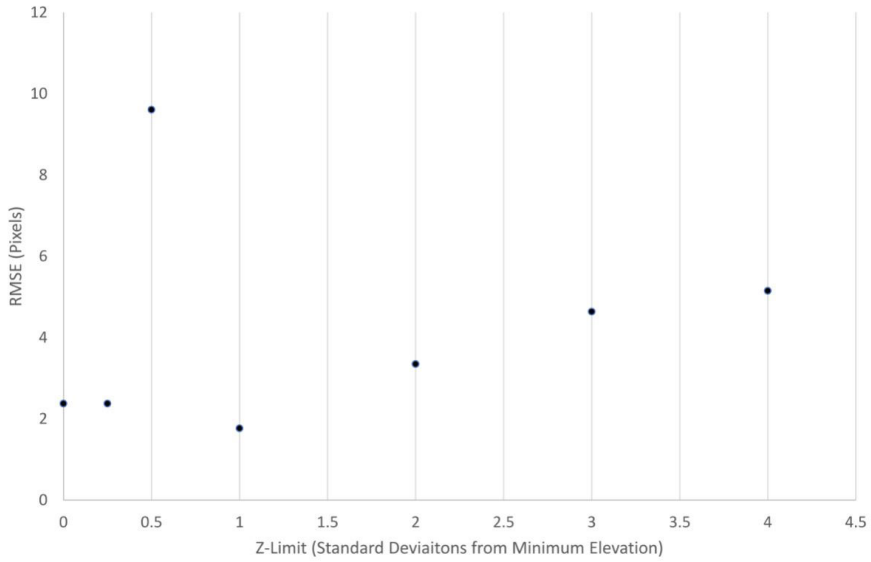

5.2. Roughness

Two indices of roughness are evaluated in this study: random roughness, which quantifies roughness per pixel in a given scene, and horizontal roughness, which quantifies roughness per class in a given scene. A sensitivity analysis of each roughness metric at different pixel resolutions allows a user to select the most appropriate one as informed by the pixel resolution of the available imagery. As mentioned above, the first step in quantifying either index is to classify land cover. This section will detail the accuracy assessment of that classification and the sensitivity analysis of random and horizontal roughness.

5.2.1. Accuracy of K-Means Classification

Each metric relied on an initial land cover classification procedure – in this case the K-Means learning algorithm was employed. A set of 256 randomly-stratified sample points was used in the accuracy assessment, which was used to compare the classification raster to visual assessment of the original orthophotography. A 2cm x 2cm vector grid was overlaid on the scene to help distinguish between pixels at transition zones between classes. The overall reported classification accuracy is 85.64% with an overall Cohen's kappa coefficient of 0.7797. An accuracy matrix reporting user's and producer's accuracy between classes and per-class kappa coefficients is provided in table 1.

Table 1: Accuracy matrix of K-Means classification.

Class	Reference Totals	Classified Totals	Number Correct	Producer's Accuracy	User's Accuracy	Kappa
Unclassified	0	0	0	---	---	---
Healthy Vegetation	54	60	53	98.15%	88.33%	0.8363
Woody Biomass/Sparse Vegetation	89	75	71	79.78%	94.67%	0.8987
Bare Soil	45	53	37	82.22%	69.81%	0.6031
Totals	188	188	161			
Overall Classification Accuracy =	*85.64%*					

Close observation of between-pixel disagreement reveals that shadows produced in the interrill regions of ploughed land and beneath senesced vegetation were increasingly misappropriated as vegetation. Furthermore, substantial bright light reflection from senesced vegetation was often misclassified as bare soil. More careful classification procedures or OBIA would be effective measures to absorb these errors.

5.2.2. Horizontal Roughness

Overall spatial variation of horizontal roughness was dependent on distribution of classified land cover. It is important to consider the observation window size in conceptualizing roughness (Marzahnet al., 2012). In order to accurately portray roughness per class in the theoretical variogram, the representative elementary area (REA) for each was calculated using moving window kriging at different sizes. The window size corresponding with the lowest RMSE of variogram fit for each class was then selected. Table 2 lists Manning's *n* values calculated for each class in relation to the autocorrelation length and derived REA of each theoretical variogram and Figure 8 plots RMSE per moving window size.

Table 2: Manning's n values derived per representative elementary area (REA) moving window kriging.

Open Water

Window Size (m)	$\tilde{\gamma}(h)$	$\tilde{\gamma}(\infty)$	RMSE	$\tilde{\rho}(h)$	*n*
0	0.5593	12.04188	0.28141	0.953554	0.078142
10	0.5593	0.197222	0.416231	-1.83589	-0.03344
15	0.5593	7.343327	0.198264	0.923836	0.076953
50	0.5593	11.52016	0.273007	0.95145	0.078058
64	0.5593	12.13111	0.278603	0.953895	0.078156
100	0.5593	12.13111	0.280161	0.953895	0.078156

Healthy Vegetation

Window Size (m)	$\tilde{\gamma}(h)$	$\tilde{\gamma}(\infty)$	RMSE	$\tilde{\rho}(h)$	*n*
0	6.2747	23.06426	0.265952	0.727947	0.135515
10	6.2747	25.59698	0.124961	0.754866	0.137938
15	6.2747	24.59151	0.186984	0.744843	0.137036
50	6.2747	11.52016	0.273007	0.455329	0.11098
65	6.2747	23.43694	0.24529	0.732273	0.135905
100	6.2747	12.13111	0.280161	0.482759	0.113448

(Table continues.)

Table 2: Manning's n values derived per representative elementary area (REA) moving window kriging (continued).

Woody Biomass

Window Size (m)	$\tilde{\gamma}(h)$	$\tilde{\gamma}(\infty)$	RMSE	$\tilde{\rho}(h)$	*n*
0	3.8351	37.61563	0.296559	0.898045	0.066432
10	3.8351	39.15367	0.111601	0.90205	0.066572
15	3.8351	38.22346	0.188819	0.899666	0.066488
50	3.8351	37.61563	0.286374	0.898045	0.066432
65	3.8351	37.61563	0.287896	0.898045	0.066432
100	3.8351	37.61563	0.291524	0.898045	0.066432

Bare Soil

Window Size (m)	$\tilde{\gamma}(h)$	$\tilde{\gamma}(\infty)$	RMSE	$\tilde{\rho}(h)$	*n*
0	6.0619	38.2245	0.226267	0.841413	0.036828
10	6.0619	39.15474	0.106897	0.845181	0.036904
15	6.0619	28.77409	0.08608	0.789328	0.035787
50	6.0619	38.53209	0.218206	0.842679	0.036854
65	6.0619	38.53209	0.218376	0.842679	0.036854
100	6.0619	12.13111	0.280161	0.500301	0.030006

Figure 8. Root-mean-square error of variogram fit per moving window size.

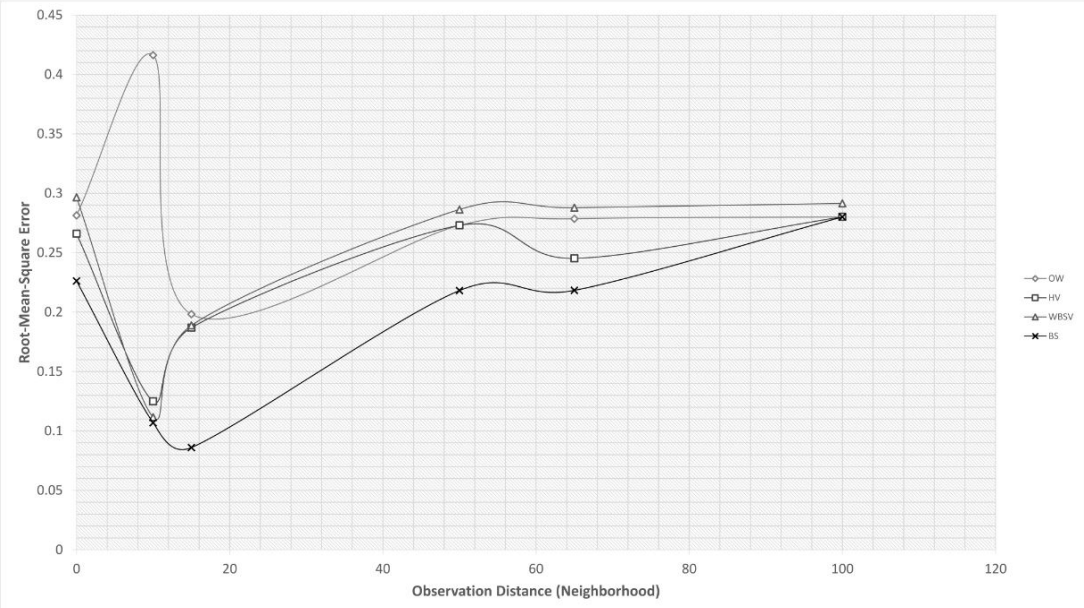

5.2.3. Random Roughness

Because the observation window of standard deviations of z-values per pixel in the DTM was specifically the immediate neighborhood (3 by 3 pixels), no sensitivity analysis was performed on the modeling of random roughness.

5.3. Hydrologic Modeling Sensitivity Analysis

To assess the variation in plots of WSE, maximum depth, and maximum velocity, all values were normalized from 0 to 100 and tested in a single factor analysis of variance (ANOVA). In this instance, the null hypothesis states that the plots generated from spatially-varying descriptions of surficial roughness are not significantly different than the *n* = 1 model. Each ANOVA demonstrated that the null hypothesis can be rejected in all three instances (the P-value approached or equaled 0 in all tests).

Next, to rule out the assumption that the *n* = 1 model was the main source of statistical variation, another set of ANOVA tests were conducted with it excluded (i.e. 15 degrees of freedom). However, the results indicate that the sources of variation do indeed lie somewhere within the scalar parameterization of roughness. Specifically, WSE had a P-value of 0.0044, maximum depth of 0, and maximum velocity of 0 – indicating extended statistical dissimilarity among the sets.

Figure 9: Roughness layers producing statistically-significant results of WSE, maximum water depth, and maximum velocity, in hydrologic modeling.

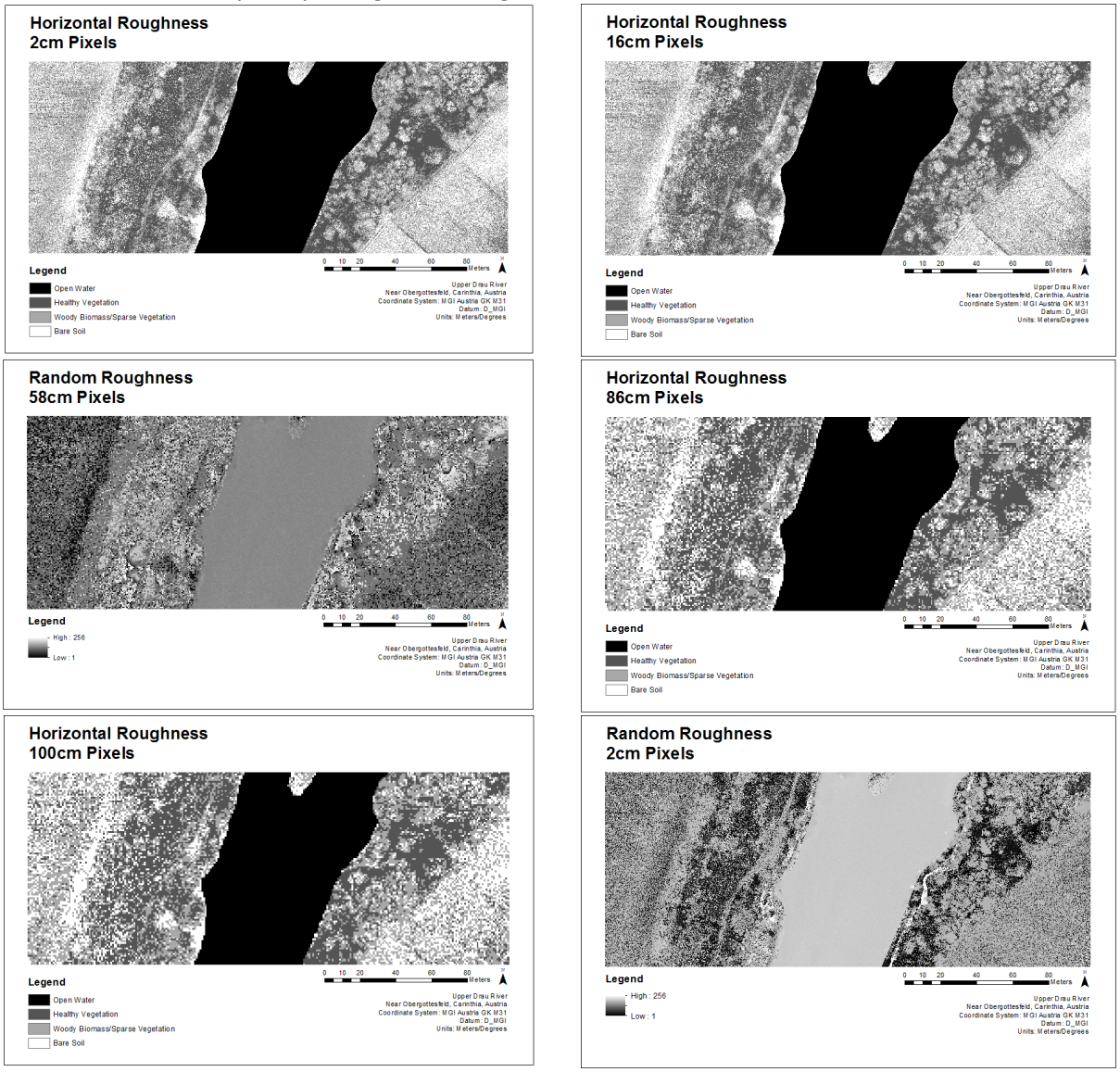

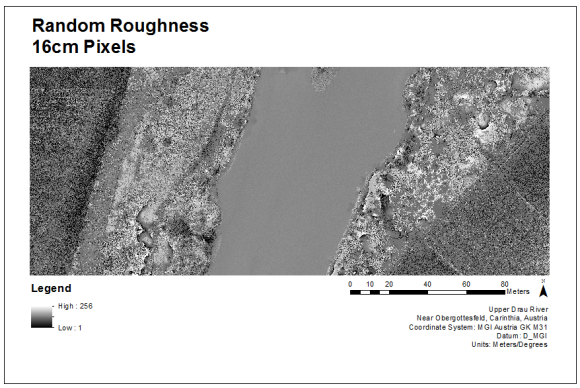

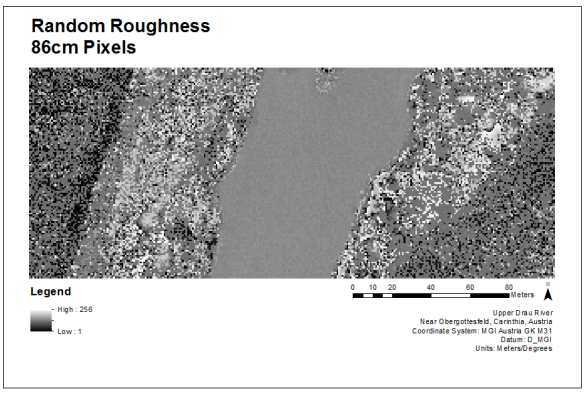

A series of two-sample t-Tests assuming unequal variances were conducted between the *n* = 1 model and each roughness scale model, iteratively. Figure 9 demonstrates every roughness layer associated with statistically significant results in the modeling process. A significant and unpredictable level of variation within and among groups was demonstrated. The strongest variance in WSE was predicted with the 2cm horizontal model, and the worst was the 16cm random model. An overall trend demonstrates that smaller pixel size is a stronger predictor of variance of WSE, with horizontal roughness typically outperforming random roughness. There was only one model for which the null hypothesis could be rejected in terms of maximum depth quantification – 16cm random roughness (Figure 10). Results were generally quite scattered, particularly among horizontal roughness models. A slight trend indicates that smaller pixel size is a stronger predictor of variance of maximum depth among random roughness models. The strongest predictor of statistical variance of maximum velocity modeling was the 16cm horizontal roughness model, and the worst predictor was the 2cm random roughness model. Furthermore, there is no clear trend associated between pixel size and maximum velocity.

Figure 10: Significance of pixel resolution on WSE quantification.

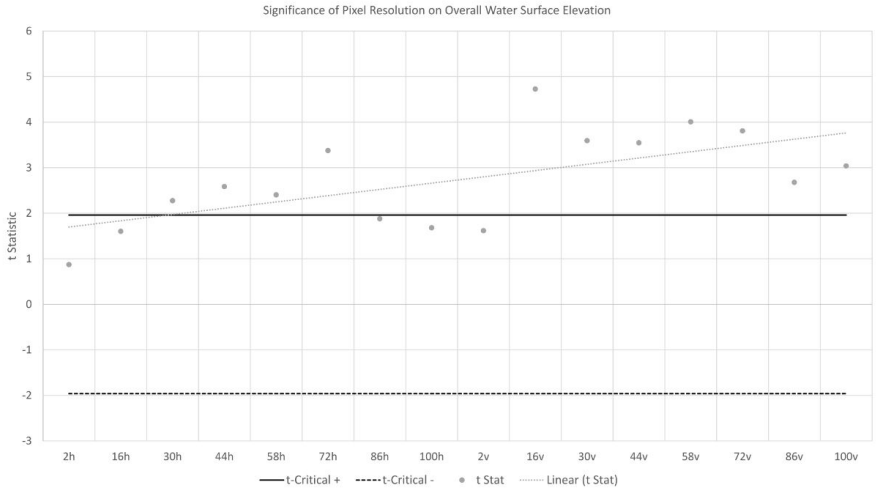

Figure 11: Significance of pixel resolution on maximum depth quantification.

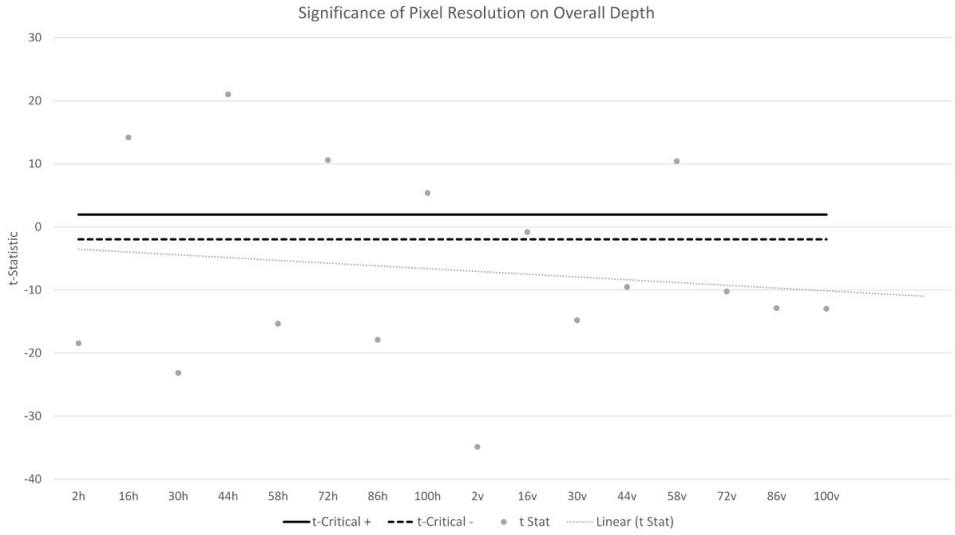

Figure 12: Significance of pixel resolution on maximum velocity quantification.

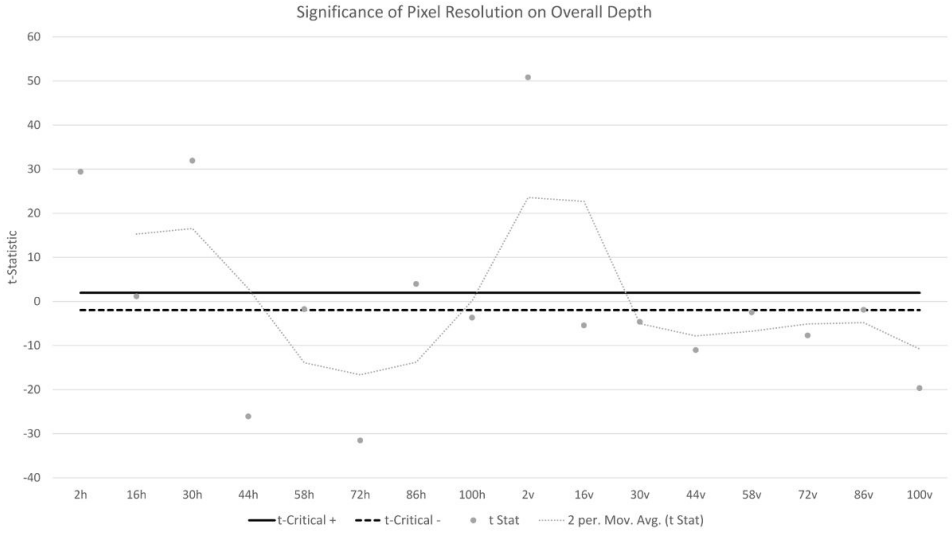

6. Discussion

In this paper a proof-of-concept structure for utilizing high-spatial resolution imagery obtained from a UAS platform to develop a distributed 2D hydraulic model of a river channel and simulated floodplain is proposed. A DSM is generated by employing the photogrammetric technique of SfM, and from this DSM a DTM is estimated using common GIS tools to within a reported RMSE of 4.65 centimeters. The effectiveness of two roughness metrics – horizontal and random roughness – to capture spatial variation of roughness as it relates to Manning's *n* coefficient and quantitative outputs in a simulated unsteady flow scenario using HEC-RAS modeling software was compared. Results indicate that accuracy in hydraulic modeling is affected by scale. However, spatial resolution is not necessarily a reliable indicator of precision across different metrics, specifically WSE, maximum depth, and maximum velocity. Each of these metrics should be considered in a contextually-sensitive manner that is determined by the user

based on the need to determine principles of structural stability of static and dynamic water catchment and flood control systems, water quality by means of particle and sediment transport, and more.

Spatial resolution also appears to have negative impacts on classification schemes, namely that differentiation between underwater features and those along the floodplain is limited. This suggests that OBIA as the classification paradigm in hydraulic modeling ought to be explored in future work. SfM and other photogrammetric or scanner-based (laser, SAR, etc.) 3D models that are becoming increasingly available can help facilitate more accurate object-based classification.

Regarding the DTM approximation, the fill technique does provide a solid foundation for future work. However, the toolset available in most GIS products is only sensitive to threshold values along the z-axis, while it might be useful to consider spatial properties of depressions as they occur along the x-y plane. Further research into applying data from a classification into zonal fills is also warranted. Furthermore, understanding classification as it relates to points along the DSM can help isolate sources of error in approximation of a DTM whereby error is likely occurring with greater frequency along pixels associated with vegetation.

Understanding the spatial variability of roughness in terms of Manning's *n* coefficients of channel conductivity and physical characteristics of elevation values is typically regarded as two separate endeavors. By relying on established scientific principles of both, this research aims to fuse the two to facilitate the inclusion of more precise metrics of spatial variability in existing hydraulic modeling packages. However, users must be aware of the levels of uncertainty that are introduced and compounded in such a process. Accuracy and accountability in data collection, classification schemes, statistical analysis, and pixel resampling, should be approached with care to ensure defensible results.

In sum, the results of the proposed proof-of-concept model indicate that users of hydrologic modeling software must exercise care when making claims regarding the accuracy of results. Referring to complexity by way of different scenarios, resilience is also context-dependent. These hydraulic models simulate flash floods along a stretch of the Drau lined with levees. The impact of a flash flood on a system with diverse levels of flood protection will vary greatly and have many different implications on processes of system or infrastructure interdependence and human equity. Researchers and practitioners must maintain situational awareness when developing models that they are adequately responsible for the complexity of the modeled system and are forthright in error approximation and reporting.

7. Conclusion

This research explores the most effective methods of utilizing aerial imagery derived from a UAS to conduct flood modeling. A sequential workflow with built-in error approximation and sensitivity analysis is presented. Proceeding from a UAS mission for data collection, the workflow covers data processing, the approximation of a DTM, generation of a roughness surface, and hydrologic modeling. A DSM is generated using SfM photogrammetric scene reconstruction in Agisoft PhotoScan (version 1.4). Because a DTM is typically required for hydrologic modeling in vegetated areas, one is approximated by using readily-available GIS modeling tools and raster math. Finally, two indices of roughness are calculated and compared in a sensitivity analysis of hydrologic model outputs. The results of the analysis indicate the most appropriate basic parameters to produce statistically-significant flood models given the spatial resolution of available imagery.

Spatially-varying models of roughness in hydraulic modeling are both possible and relatively straightforward – the implications of which can be extended to more complex geometric inputs in the hydraulic modeling process, for example more detailed break lines and grid cells with complex structures, such as bridge or building foundations, weirs, dams, culverts, and depression or storage areas. Care must be taken in more complex modeling scenarios to ensure that input environments are as representative of reality as possible to ensure accurate model measurements.

8. Future Work and Outlook

A limiting factor in the development of precise dynamic hydrologic models based on high-resolution UAS data is the ability of computational systems to handle robust datasets. Future work ought to focus on modeling longer stretches of channel and associated floodplains, both to examine the feasibility of modern computer technology in handling the necessary data, and to explore the results of a larger array of spatial variability.

The real-world implications derived from the sensitivity analysis portion of the current research hinges on the reported accuracy of the HEC-RAS modeler. May, Lopez, and Brown (2000) demonstrated that surface water models in open channel scenarios have relatively high accuracy (1.2% validation error), but that accuracy diminishes precipitously as slope increases. Conversely, the U.S. Army Corps of Engineers identifies user input error in defining tolerances as a direct influencer of model precision (U.S. Army Corps of Engineers, 2016). Parameters relating to structural impedances to flow and cross-sectional modeling of hydraulic gradients are often-overlooked variables which can lead to further reduction in validity (Thomas and Williams, 2007). Rigorous model design is necessary to reduce the number of “free” parameters as possible that require external calibration (Refsgaard, 1997). Therefore, relatively simplistic parameters were set and applied uniformly across all model iterations during sensitivity analysis. This calls for a systematic analysis of the inclusion of more parameters in the modeling process coupled with a statistical evaluation similar to the one presented in this paper.

9. References

Achleitner, S. & Rauch, W. (2006). Increase of River Base Flow by Hydropower Gate Operation for Mitigation of CSO Impacts – Potential and Limitations. *Water Resources Management, 21,* 1487-1503.

Agisoft LLC. (2018). *Agisoft PhotoScan User Manual: Professional Edition, Version 1.4*.

Allmaras, R. R., Burwell, R. E., Larson, W. E., Holt, R. F., & Nelson, W. W. (1966). *Total Porosity and Random Roughness of the Interrow Zone as Influenced by Tillage*. Washington, D.C.: U.S. Government Printing Office.

Auer, I., Böhm, R., Hofstätter, M., Türk, K., & Kottek, M. (2011). *Long-Term Climate of Carinthia: Historical climate trends, future scenarios and climate change indices for the province of Carinthia* Vienna: ZAMG

Blaes, X., & Defourny, P. (2008). Characterizing Bidimensional Roughness of Agricultural Soil Surfaces for SAR Modeling. *IEEE Transactions on Geoscience and Remote Sensing, 46*(12), 4050-4061.

Boiffin, J. (1984). La dégradation structurale des couches superficielles du sol sous l'action des pluies. Thèse de Docteur-Ingénieur, Inst. Natl. Agr., Paris.

Chou, C. and Tseng, S. (2010). Collection and Analysis of Critical Infrastructure Interdependency Relationships. *Journal of Computing in Civil Engineering*, 24(6): 539-47.

Chow, V.T. (1959). Open-channel hydraulics. New York, McGraw-Hill, 680 p.

Clark, M. P., Bierkens, M. F. P., Samaniego, L., Woods, R. A., Uijlenhoet, R., Bennett, K. E., . . . Peters-Lidard, C. D. (2017). The evolution of process-based hydrologic models: historical challenges and the collective quest for physical realism. *Hydrology and Earth System Sciences, 21*, 3427-3440.

Copeland, R. R. (2000). *Determination of Flow Resistance Coefficients Due to Shrubs and Woody Vegetation*. Vicksburg, MS.: U.S. Army Engineer Research and Development Center.

Currence, H., & Lovely, W. (1970). The Analysis of Soil Surface Roughness. *Transactions of the ASAE, 13*, 710-714.

Davidson, M. W. J., Toan, T. L., Mattia, F., Satalino, G., Manninen, T., & Borgeaud, M. (2000). On the Characterization of Agricultural Soil Roughness for Radar Remote Sensing Studies. *IEEE Transactions on Geoscience and Remote Sensing, 38*(2), 630-640.

Dorn, H., Vetter, M., & Hölfe, B. (2014). GIS-Based Roughness Derivation for Flood Simulations: A Comparison of Orthophotos, LiDAR and Crowdsourced Geodata. *Remote Sensing, 6*, 1739-1759.

Drava River Floods Hundreds of Homes. (2012). *The Slovenian Times*. Retrieved from http://www.sloveniatimes.com/drava-river-floods-hundreds-of-homes

Jenness, J. (2013). Topographic Position Index (tpi_jen.avx) extension for ArcView 3.x, v. 1.2. Jenness Enterprises. Available at: http://www.jennessent.com/arcview/tpi.htm.

Kamphorst, E. C., Jetten, V., Guérif, J., Pitkänen, J., Iverson, B. V., Douglas, J. T., & Paz, A. (2000). Predicting Depressional Storage from Soil Surface Roughness. *Soil Science Society of America Journal, 64*, 1749-1758.

Langhammer, J. B., J., & Mirijovský, J. (2017). Building a High-Precision 2D Hydrodynamic Flood Model Using UAV Photogrammetry and Sensor Network Monitoring. *Water, 9*(861), 1-22.

Leavitt, W. and Kiefer, J. (2006). Infrastructure Interdependencey and the Creation of a Normal Disaster:

The Case of Hurricane Katrina and the City of New Orleans. *Public Works Management & Policy, 10(4),* 306-314.

Lebensader Obere Drau (2011). *LIFE-Project: Life vein – Upper Drau River.* Carinthian State Government, Austria.

López, P., Sutanudjaja, E., Schellekens, J., Sterk, G., & BierkensM. (2017). Calibration of a large-scale hydrological model using satellite-based soil moisture and evapotranspiration products *Hydrology and Earth System Sciences, 21*, 3125-3144.

Luo, X., Hong, Y., Lei, X., Leung, L. R., Li, H., & Getirana, A. (2017). *An Investigation on the Spatial Variability of Manning Roughness Coefficients in Continental-scale River Routing Simulations*. Paper presented at the AGU Fall Meeting, New Orleans, LA.

Marzahn, P., & Ludwig, R. (2009). On the derivation of soil surface roughness from multi parametric PolSAR data and its potential for hydrological modeling. *Hydrology and Earth System Sciences, 13*, 381-394.

Marzahn, P., Rieke-Zapp, D., & Ludwig, R. (2012). Assessment of soil surface roughness statistics for microwave remote sensing applications using a simple photogrammetric acquisition system. *ISPRS Journal of Photogrammetry and Remote Sensing, 72*, 80-89.

May, D., Lopez, A., & Brown, L. (2000). *Validation of the Hydraulic-Open Channel Flow Model HEC-RAS with Observed Data*. Unpublished Manuscript.

Niedzielski, T., Witek, M., & Spallek, W. (2016). Observing river stages using unmanned aerial vehicles. *Hydrology and Earth System Sciences, 20*, 3193-3205.

Ouyang, M. (2014). Review on modeling and simulation of interdependent critical infrastructure systems. *Reliability Engineering and System Safety, 121*, 43-60.

Refsgaard, J. C. (1997). Parameterisation, calibration and validation of distributed hydrological models *Journal of Hydrology, 198*, 69-97.

Robert, B., Senay, M., Plamondon, M. P., & Sabourin, J. (2003). *Characterization and Ranking of Links Connecting Life Support Networks*. Ottawa, ON: Her Majesty the Queen in Right of Canada.

Taconet, O., & Ciarletti, V. (2007). Estimating soil roughness indices on a ridge-and-furrow surface using stereo photogrammetry. *Soil and Tillage Research, 93*, 64-76.

Thomas, I. M., & Williams, D. T. (2007). *Common Modeling Mistakes Using HEC-RAS*. Paper presented at the World Environmental and Water Resources Congress 2007: Restoring Our Natural Habitat, Tampa, FL.

Tokarczyk, P., Leitao, J. P., Rieckermann, J., Schindler, K., & Blumensaat, F. (2015). High-quality observation of surface imperviousness for urban runoff modelling using UAV imagery. *Hydrology and Earth System Sciences, 19*, 4215-4228.

U.S. Army Corps of Engineers, (2016). *HEC-RAS River Analysis System 2D Modeling User's Manual*. Davis, CA.

Verhoest, N. E. C., Lievens, H., Wagner, W., Álvarez-Mozoz, J., Moran, M. S., & Mattia, F. (2008). On the Soil Roughness Parameterization Problem in Soil Moisture Retrieval of Bare Surfaces from Synthetic Aperture Radar. *Sensors, 8*, 4213-4248.

Vivoni, E. R., Rango, A., Anderson, C. A., Pierini, N. A., Schreiner-McGraw, A. P., Saripalli, S., & Laliberte, A. S. (2014). Ecohydrology with unmanned aerial vehicles. *Ecosphere, 5*(10), 1-14.

Webster, R., & Oliver, M. (2007). *Geostatistics for Environmental Scientists*. Cornwall: Wiley.

Zhang, S., & Liu, Y. (2017). Experimental Study on Anisotropic Attributes of Surface Roughness in Watersheds. *Journal of Hydrologic Engineering, 22*(11), 1-6.

Zhang, S., Liu, Y., Zhang, J., Liu, Y., & Wang, Z. (2018). Theory and preliminary experimental verification of the directional difference of overland flow resistance in distributed hydrological models (uncorrected proof). *Water Science & Technology: Water Supply, In Press*.

Zhang, S., Liu, Y., Li, M., & Liang, B. (2016). Distributed hydrological models for addressing effects of spatial variability of roughness on overland flow. *Water Science and Engineering, 9*(3), 249-255.

10. Appendix 1 – Roughness Layers

Horizontal Roughness 2cm Pixels

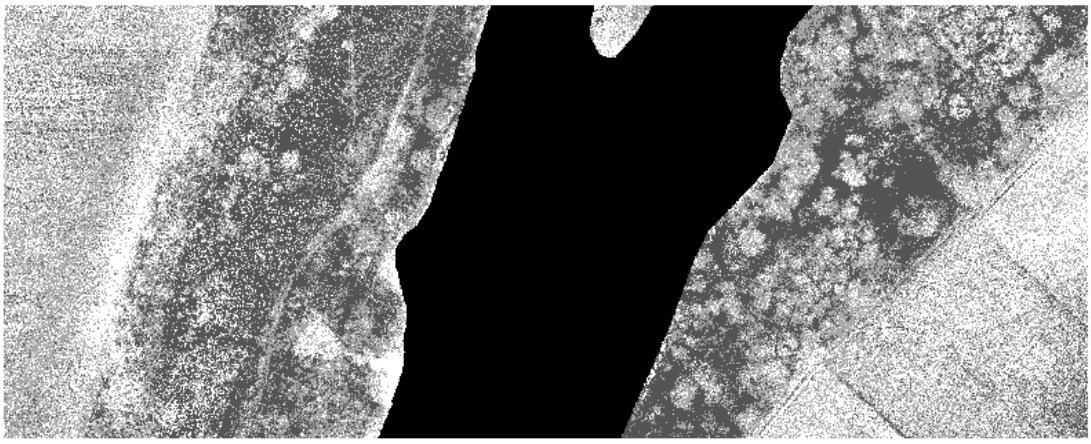

0 10 20 40 60 80 Meters

Legend

- Open Water
- Healthy Vegetation
- Woody Biomass/Sparse Vegetation
- Bare Soil

Upper Drau River
Near Obergottesfeld, Carinthia, Austria
Coordinate System: MGI Austria GK M31
Datum: D_MGI
Units: Meters/Degrees

Horizontal Roughness 16cm Pixels

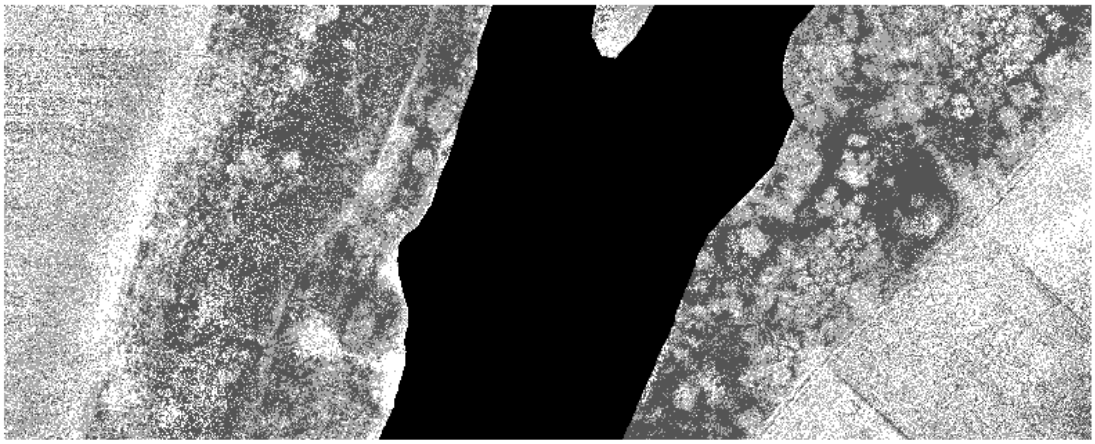

0 10 20 40 60 80 Meters

Legend

- Open Water
- Healthy Vegetation
- Woody Biomass/Sparse Vegetation
- Bare Soil

Upper Drau River
Near Obergottesfeld, Carinthia, Austria
Coordinate System: MGI Austria GK M31
Datum: D_MGI
Units: Meters/Degrees

Horizontal Roughness
30cm Pixels

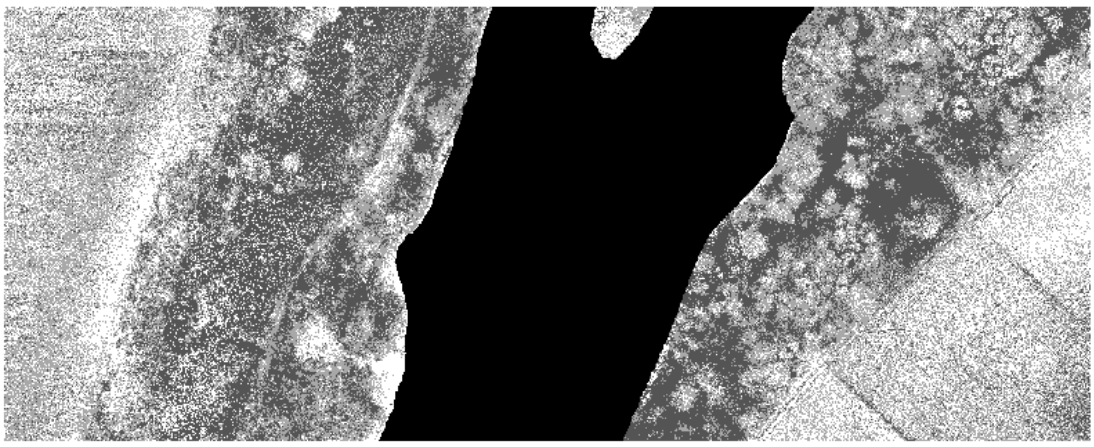

0 10 20 40 60 80
Meters

N

Legend

- Open Water
- Healthy Vegetation
- Woody Biomass/Sparse Vegetation
- Bare Soil

Upper Drau River
Near Obergottesfeld, Carinthia, Austria
Coordinate System: MGI Austria GK M31
Datum: D_MGI
Units: Meters/Degrees

Horizontal Roughness
44cm Pixels

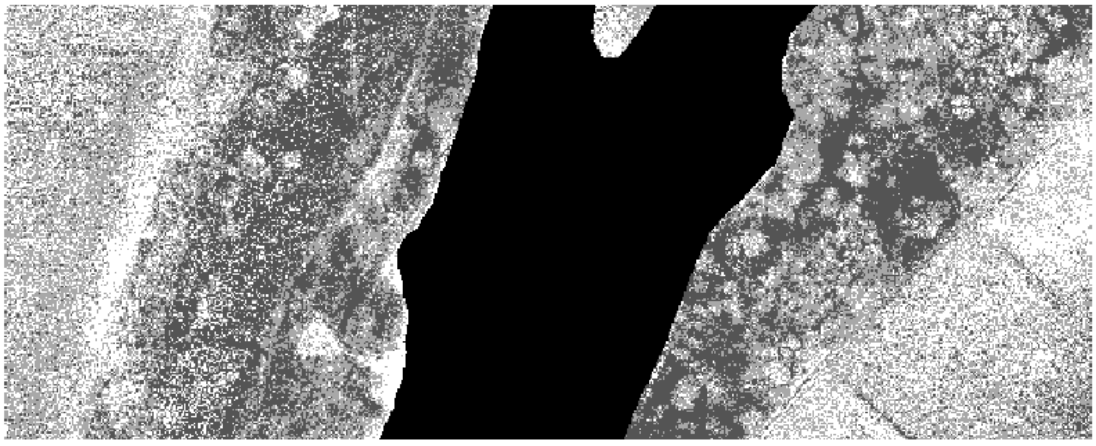

0 10 20 40 60 80
Meters

N

Legend

- Open Water
- Healthy Vegetation
- Woody Biomass/Sparse Vegetation
- Bare Soil

Upper Drau River
Near Obergottesfeld, Carinthia, Austria
Coordinate System: MGI Austria GK M31
Datum: D_MGI
Units: Meters/Degrees

Horizontal Roughness
58cm Pixels

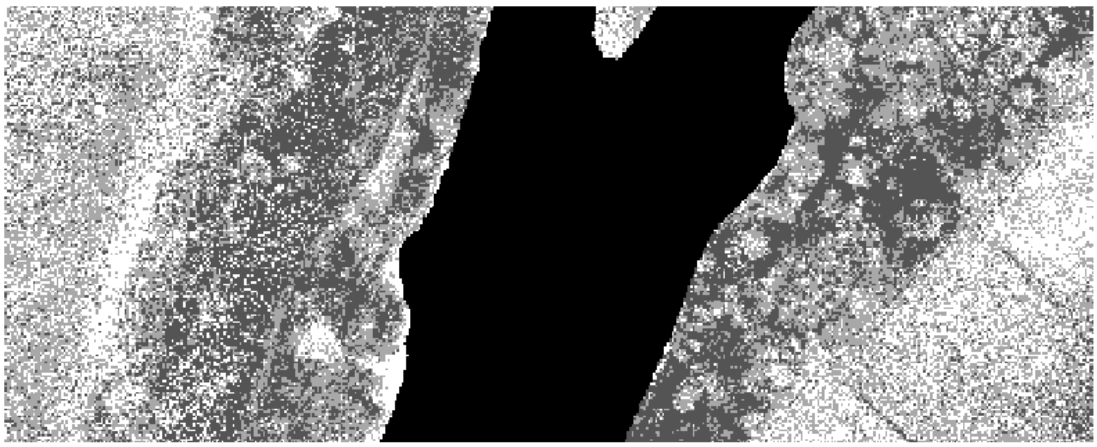

0 10 20 40 60 80 Meters

Legend

- Open Water
- Healthy Vegetation
- Woody Biomass/Sparse Vegetation
- Bare Soil

Upper Drau River
Near Obergottesfeld, Carinthia, Austria
Coordinate System: MGI Austria GK M31
Datum: D_MGI
Units: Meters/Degrees

Horizontal Roughness
72cm Pixels

0 10 20 40 60 80 Meters

Legend

- Open Water
- Healthy Vegetation
- Woody Biomass/Sparse Vegetation
- Bare Soil

Upper Drau River
Near Obergottesfeld, Carinthia, Austria
Coordinate System: MGI Austria GK M31
Datum: D_MGI
Units: Meters/Degrees

Horizontal Roughness
86cm Pixels

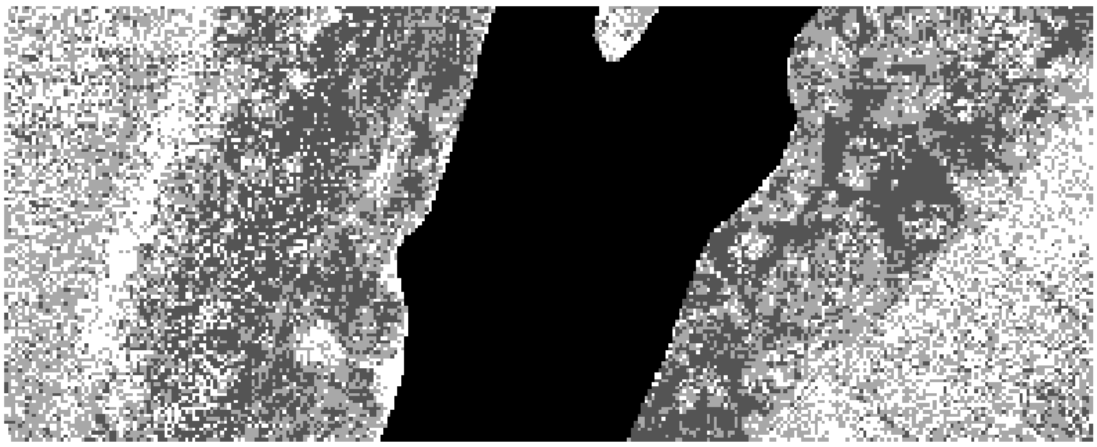

0 10 20 40 60 80 Meters

N

Legend

- Open Water
- Healthy Vegetation
- Woody Biomass/Sparse Vegetation
- Bare Soil

Upper Drau River
Near Obergottesfeld, Carinthia, Austria
Coordinate System: MGI Austria GK M31
Datum: D_MGI
Units: Meters/Degrees

Horizontal Roughness
100cm Pixels

0 10 20 40 60 80 Meters

N

Legend

- Open Water
- Healthy Vegetation
- Woody Biomass/Sparse Vegetation
- Bare Soil

Upper Drau River
Near Obergottesfeld, Carinthia, Austria
Coordinate System: MGI Austria GK M31
Datum: D_MGI
Units: Meters/Degrees

Random Roughness
2cm Pixels

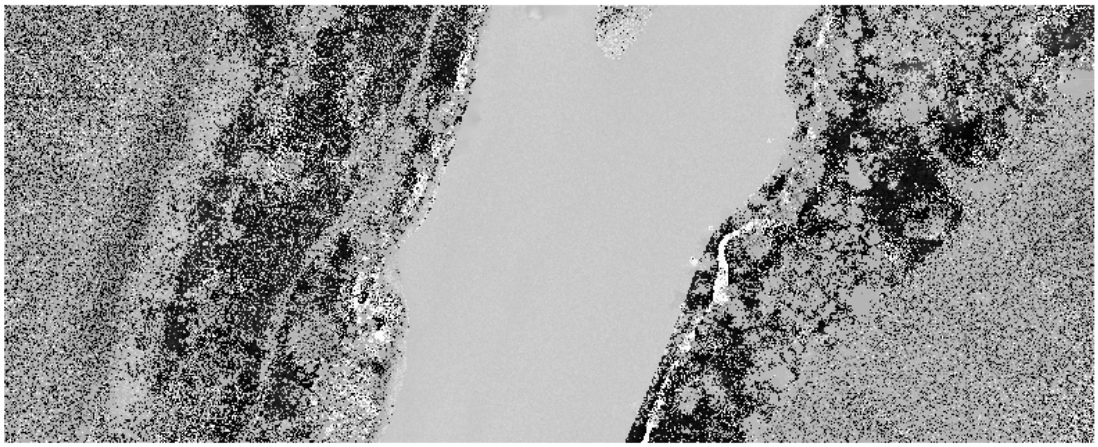

Legend

High : 256

Low : 1

0 10 20 40 60 80
Meters

N

Upper Drau River
Near Obergottesfeld, Carinthia, Austria
Coordinate System: MGI Austria GK M31
Datum: D_MGI
Units: Meters/Degrees

Random Roughness
16cm Pixels

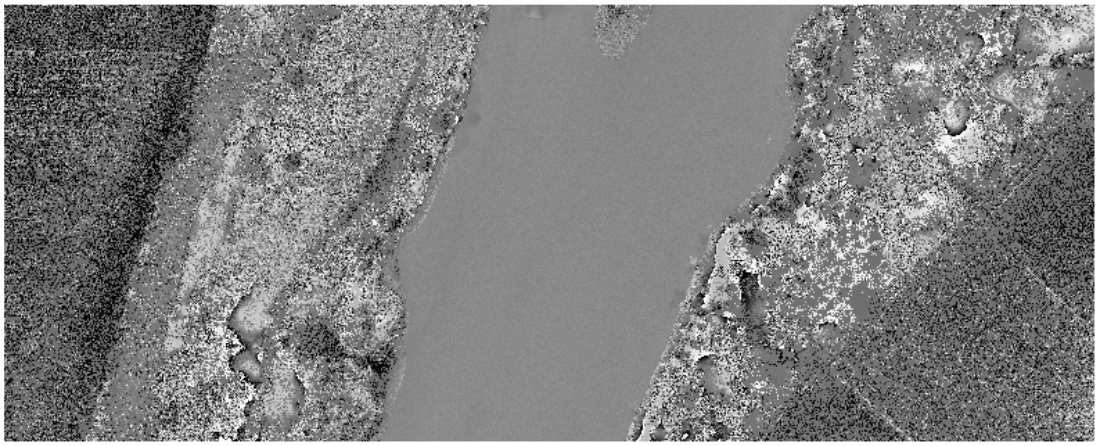

Legend

High : 256

Low : 1

0 10 20 40 60 80
Meters

N

Upper Drau River
Near Obergottesfeld, Carinthia, Austria
Coordinate System: MGI Austria GK M31
Datum: D_MGI
Units: Meters/Degrees

Random Roughness
30cm Pixels

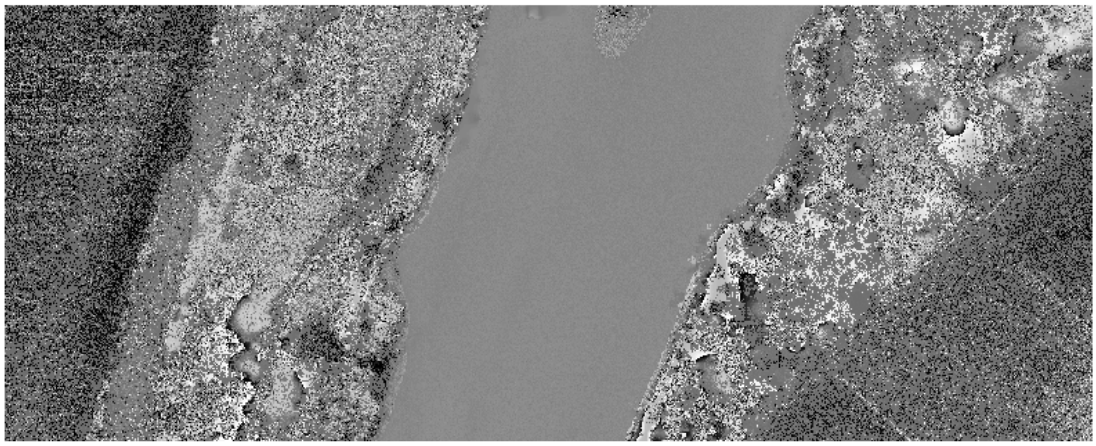

Legend

High : 256

Low : 1

0 10 20 40 60 80
Meters

N

Upper Drau River
Near Obergottesfeld, Carinthia, Austria
Coordinate System: MGI Austria GK M31
Datum: D_MGI
Units: Meters/Degrees

Random Roughness
44cm Pixels

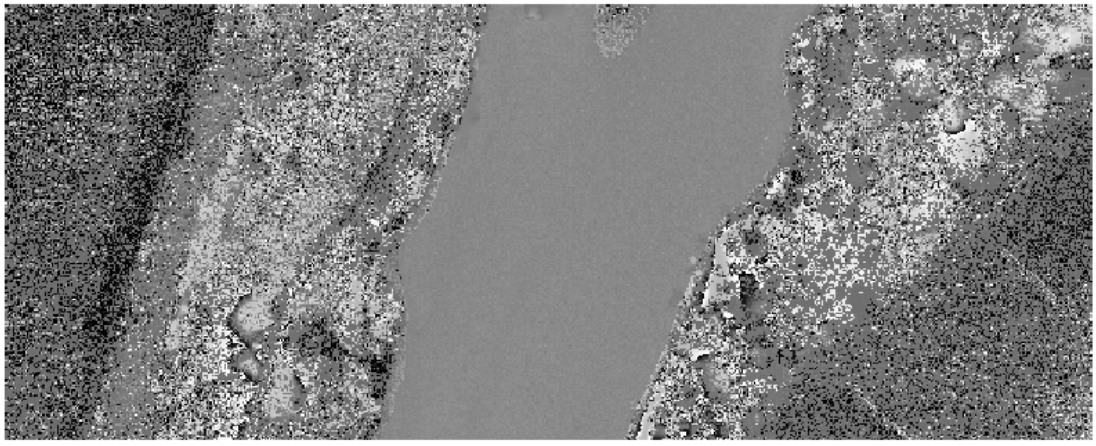

Legend

High : 256

Low : 1

0 10 20 40 60 80
Meters

N

Upper Drau River
Near Obergottesfeld, Carinthia, Austria
Coordinate System: MGI Austria GK M31
Datum: D_MGI
Units: Meters/Degrees

Random Roughness
58cm Pixels

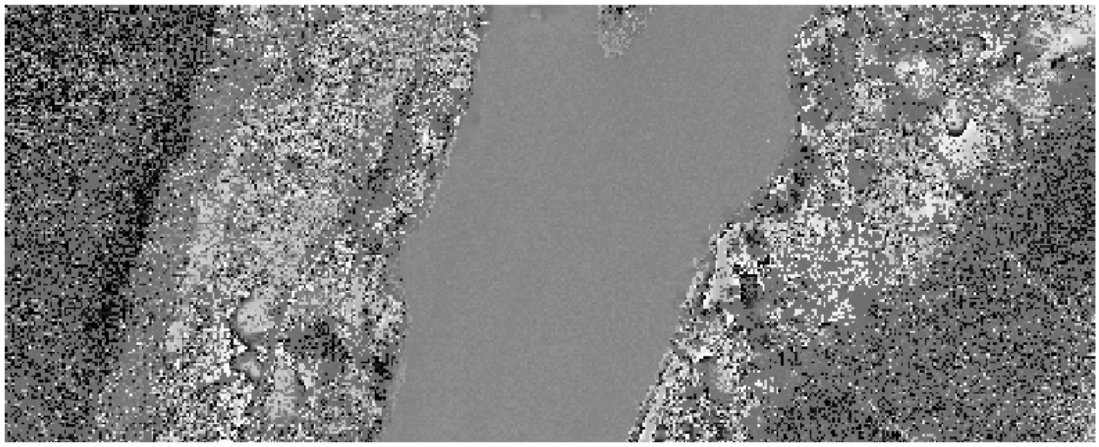

Legend

High : 256

Low : 1

0 10 20 40 60 80
Meters

N

Upper Drau River
Near Obergottesfeld, Carinthia, Austria
Coordinate System: MGI Austria GK M31
Datum: D_MGI
Units: Meters/Degrees

Random Roughness
72cm Pixels

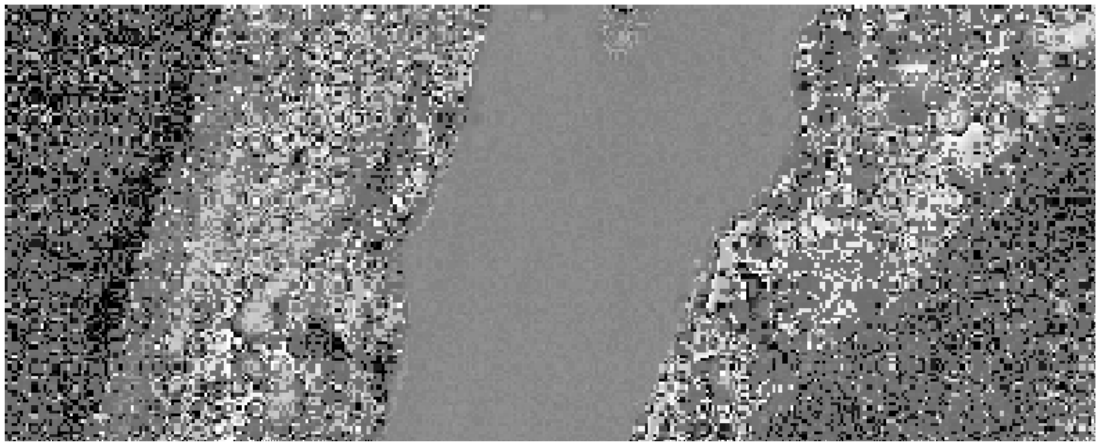

Legend

High : 256

Low : 1

0 10 20 40 60 80
Meters

N

Upper Drau River
Near Obergottesfeld, Carinthia, Austria
Coordinate System: MGI Austria GK M31
Datum: D_MGI
Units: Meters/Degrees

Random Roughness
86cm Pixels

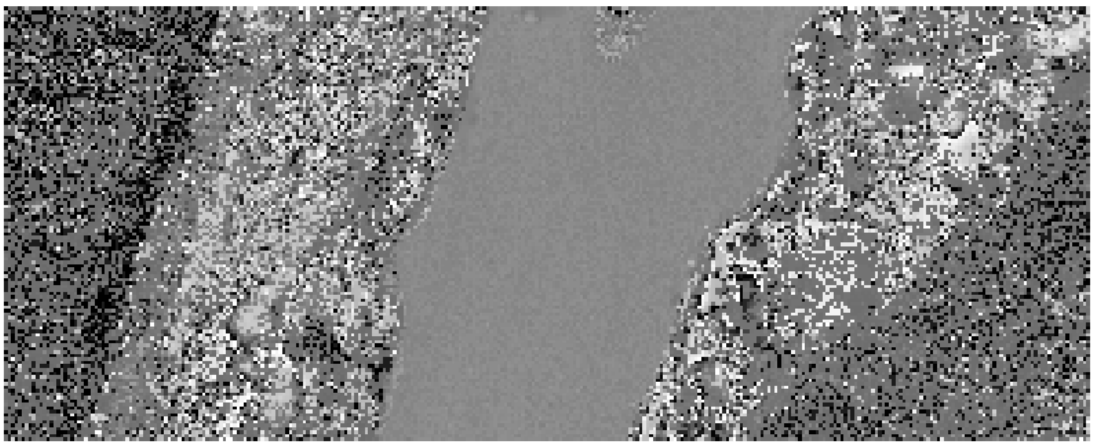

Legend

High : 256

Low : 1

0 10 20 40 60 80 Meters

N

Upper Drau River
Near Obergottesfeld, Carinthia, Austria
Coordinate System: MGI Austria GK M31
Datum: D_MGI
Units: Meters/Degrees

Random Roughness
100cm Pixels

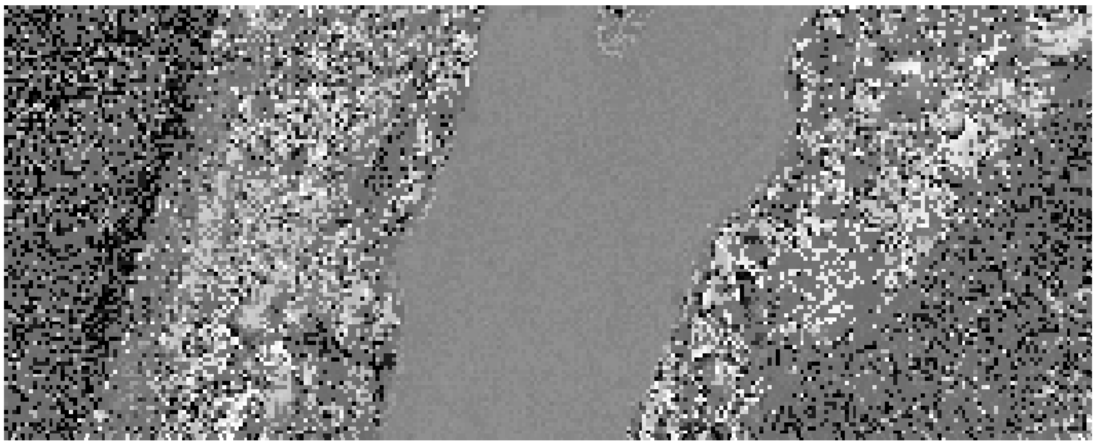

Legend

High : 256

Low : 1

0 10 20 40 60 80 Meters

N

Upper Drau River
Near Obergottesfeld, Carinthia, Austria
Coordinate System: MGI Austria GK M31
Datum: D_MGI
Units: Meters/Degrees